JOURNAL OF MATERIALS SCIENCE **38** (2003) 565–573

An investigation of oxidation effects on hysteresis heating of nickel particles

W. SUWANWATANA*,‡
*Center for Composite Materials and Department of Material Science and Engineering, University of Delaware, Newark DE, 19716, USA

S. YARLAGADDA
Center for Composite Materials, University of Delaware, Newark DE 19716, USA

J. W. GILLESPIE JR.
*Center for Composite Materials and Department of Material Science and Engineering, University of Delaware, Newark DE, 19716, USA
E-mail: gillespie@ccm.udel.edu

The oxidation kinetics of nickel particles with approximate diameters of 79 nm, 0.7 micron, and 3 micron, at temperatures between 250°C and 350°C in air were investigated. Thermogravimetric measurements indicated a diffusion-controlled mechanism for the oxidation of spherical metal particles. Deviation of the oxidation kinetic rate from the diffusion-limited model was found in the case of Ni 3 micron and Ni 79 nm. The oxidation rate constant is governed by an Arrhenius equation as expected. Apparent activation energies are approximately 1.55 eV, 1.32 eV and 1.12 eV for Ni 79 nm, Ni 0.7 μm and Ni 3 μm, respectively. The exponential factor is found to be a function of particle size. Oxidation maps were constructed to relate the degree of oxidation to time and temperature. The oxide formed on the surface of the particles significantly modified the magnetic properties of the nickel particles by changing both the magnetization and the coercivity. The measured properties of oxidized particles were used to construct magnetic property maps to help determine appropriate processing conditions and predict oxidation effects on hysteresis heating performance.

1. Introduction

Ferromagnetic particles are a potential candidate as susceptor materials in induction based hysteresis heating and Curie temperature based control for processing applications in composite materials [1–4]. These particles are typically impregnated in a polymer resulting in a paste-type adhesive in case of thermosets or a particulate-loaded film in thermoplastic polymers. Good mixing and uniform dispersion of particles in the polymer can be achieved by high temperature shear mixing, especially in thermoplastics. However, during the high temperature mixing process, the high particulate surface areas could lead to significant absorption of oxygen. The oxidation of the metal particles is the main degradation mechanism, which leads to a decreasing ferromagnetic performance. In order to determine appropriate processing conditions or the effect of typical polymer processing conditions on the particulate properties, it is necessary to understand the oxidation characteristics of metal particles and its effects on the magnetic properties.

Thermal oxidation of bulk metals and thin films has been studied in great detail [5–10]; however, oxidation of metal particles has been studied to a lesser extent. Theories based on diffusion [11] and on the coupled currents approach [12] have been suggested. In order to obtain an understanding of thermal oxidation of particles Karmhag *et al.* [13–15] have recently initiated fundamental studies of the oxidation kinetics of nickel particles of various sizes. In this work, we studied oxidation kinetics of nickel particles based on the thermogravimetric method. Our results on oxidation kinetic for particles with diameter of 79 nm, 0.7 micron, and 3 micron at temperature between 250°C and 350°C are compared to oxidation kinetics published in the literatures for nickel particles ranging from near macroscopic sizes (around 100 μm) [11, 13] to nanoparticles (20 nm) [15, 16] from room temperature to 1000°C. The oxidation rates in this study fall within reported limits and agree with other studies. It is seen that the presence of the oxide significantly decreases the magnetic properties of the nickel particles and hence is a key factor for optimal processing of susceptor films needed for induction processing.

2. Experimental procedures

2.1. Sample characterization

Three different sizes of Ni particles were used in this experiment. Argonide Corporation supplied the

nanometer-sized nickel powders. The micron-sized nickel particles were obtained from Cerac Incorporated. The particles were observed under a high-resolution transmission electron microscope (HRTEM) to determine their shape and size distribution. A micrograph of a collection of particles of each size is shown in Fig. 1. The particles are approximately spherical in shape and have diameters of 79.41 ± 13.21 nm, 0.73 ± 0.22 μm, and 3.40 ± 1.09 μm. As shown below, agglomerates of particles are frequently found in all three samples, which is one of the reasons for using a shear mixing process for dispersion in the polymer. The crystal structure of the particles was verified by x-ray diffraction, which also showed all the diffraction peaks for nickel, and none corresponding to oxides.

2.2. Oxidation study

A DuPont 951 thermogravimetric Analyzer (TGA) was used in the oxidation study. The nickel particles were oxidized in a platinum pan that was suspended from a quartz rod. The experiments were performed at 250, 275, 300, 325, and 350°C. About 30 mg of particles were placed in the weighed pan. The volume ratio between particles and pan is approximately 0.05. The thermocouple was positioned close to the sample. The sample and counterweight were then heated, at a rate of 25°C/min, up to the oxidation temperature with a linear argon flow of 90 mm^3/min over both assemblies. Once the oxidation temperature was reached, the atmosphere was changed to air at the same flow rate. Since it was impossible to calculate exactly when the air replaced Argon in contact with the sample, zero time was associated with the first recorded weight gain in the balance. Oxidation then proceeded isothermally for 3 hours. Since the purpose of this experiment is to study the extent of oxidation while the particles are processed in the particulate polymer film fabrication, the complete oxidation reaction was not pursued.

2.3. Magnetic properties measurement

A LakeShore Model 9300 Cryogenic Vibrating Sample Magnetometer (VSM) was used to characterize magnetic properties of nickel particles before and after oxidation. The sample under investigation was placed in a sample holder and centered between the poles of the magnet. The moment calibration of VSM is traditionally performed with a Ni standard at applied field above the saturation field of nickel, nominally 5000 Oe. The estimated accuracy of each determination is $\pm 2\%$. The magnetic properties related to hysteresis heating performance of nickel particles, i.e., Saturation Magnetization (M_s), Coercivity (H_c) and Hysteresis loop area, were calculated from the measurement of moment versus applied field.

3. Results and discussions

3.1. Oxidation kinetics

The purpose of the oxidation study is to obtain a better understanding of oxidation characteristics of ultrafine nickel particles and the effects of oxidation on their magnetic properties. The results from the TGA measurements performed at different temperatures

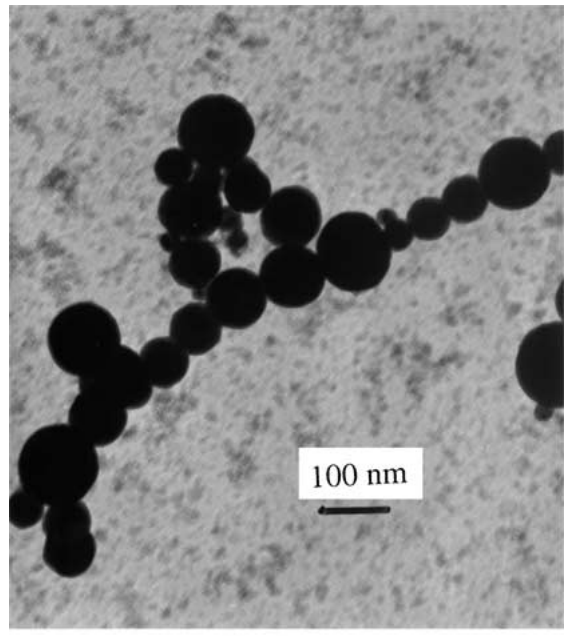

(a) Ni 79 nm

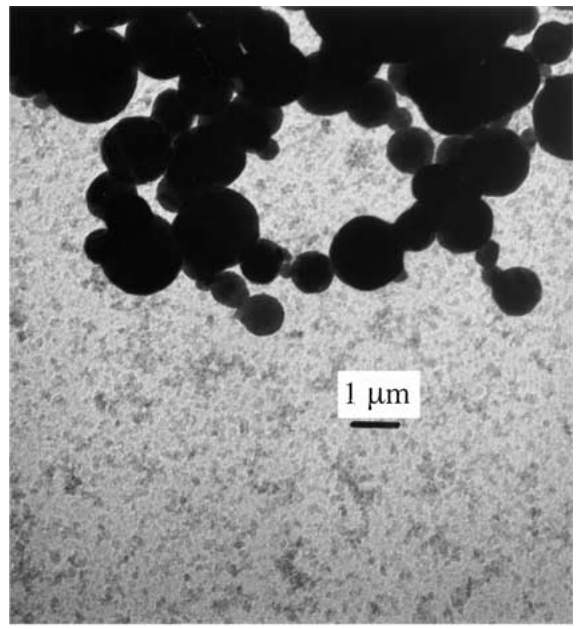

(b) Ni 0.7 μm

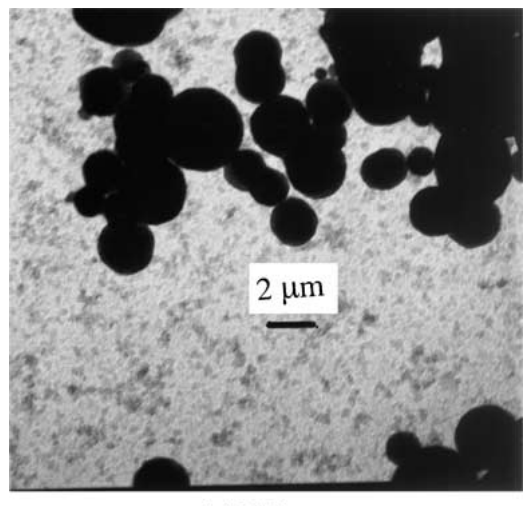

(c) Ni 3 μm

Figure 1 TEM micrographs of a collection of nickel particles at 100000× (a), 10000× (b), and 5000× (c) magnification, respectively.

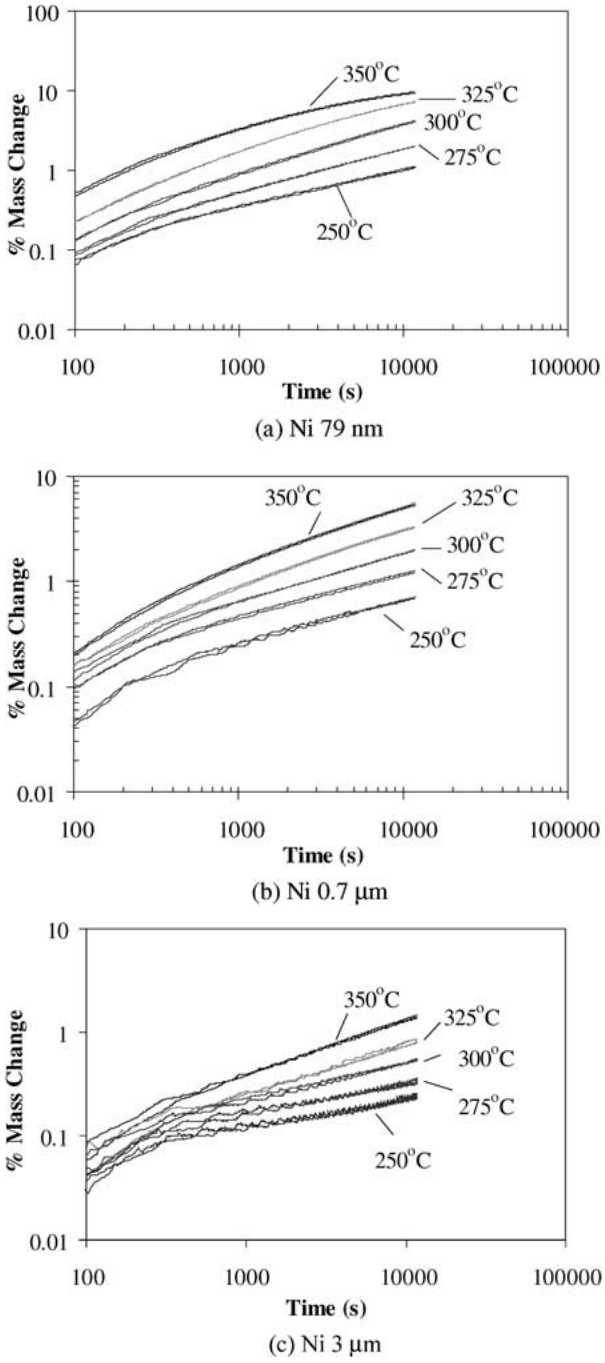

Figure 2 Percentage mass change as a function of time for oxidation of nickel 79 nm (a), 0.7 μm (b), and 3 μm (c).

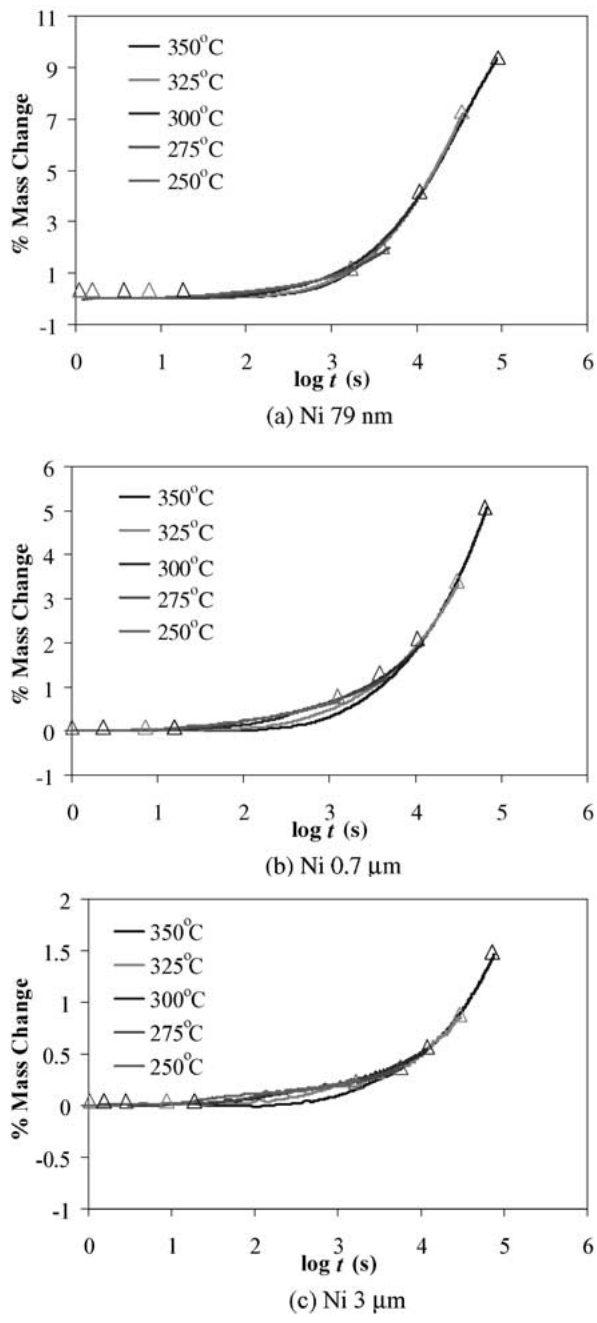

Figure 3 Master plot of oxidation kinetics curves from Fig. 2 for nickel 79 nm (a), 0.7 μm (b), and 3 μm (c) where the first and the last data point of each isotherm is marked.

between 250°C and 350°C for three hours are shown in Fig. 2a–c, where the mass change in percent is plotted versus time. The plots show two oxidation curves at each temperature and the reproducibility is seen to be very good. The experimental error is around 0.25%.

The time-temperature superposition principle is expected to hold for most theories of metal oxidation [5, 13, 14]. This principle states that the functional form at different temperatures is the same apart for a change of the time scale. If the proposition holds exactly, each isotherm in percent mass change versus time plot should coincide with the adjacent ones upon translation along the time axis, and the choice of reference point for the translation should be arbitrary. The isotherms of each particle sizes were translated about the 300°C isotherms. The resulting master plots of each particle size are shown in Fig. 3. It is shown that the oxidation kinetic of each particle size can be approximated by a single curve. The amount of displacements of the experimental data is called "shift factor" (a_T).

The activation energy of the oxidation process can be obtained from the logarithm of the shift factor (a_T) versus the inverse temperature plot in Fig. 4. The data fall on a straight line, and activation energy of metal oxidation are approximately 1.55 eV, 1.32 eV and 1.12 eV for Ni 79 nm, Ni 0.7 μm and Ni 3 μm, respectively. This method validates the time-temperature superposition principle for metal oxidation. Our value of activation energy in this temperature range lies below the value of 1.78 eV reported by Atkinson and Taylor [17] for grain boundary diffusion in NiO and 1.6 eV reported for oxidation of polycrystalline bulk nickel at

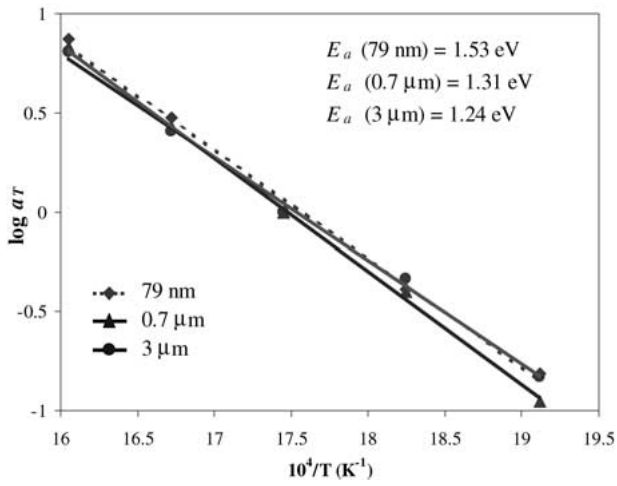

Figure 4 The logarithm of the shift factor (a_T) of the oxidation kinetics master curves (see Fig. 3) is shown as a function of inverse temperature. The activation energies E_a given in the figure were obtained from the linear fits to the data.

573–873 K [8]. However, the values found in this study range from 1.24 eV to 1.53 eV for Ni 3 μm to 79 nm are comparable to the values of 1.5 eV for 5 μm nickel particles and 1.2 eV for nickel 149 μm both reported by Kamharg *et al*. [13, 14].

The experimental data on oxidation kinetics of nickel particles are now compared to a theoretical model. Carter [11] developed the oxidation rate law for spherical nickel particles using diffusion controlled approach and expressed the rate constant in terms of the limitation of diffusion through the oxide film formed on spherical nickel particles:

$$\frac{z}{z-1} - (1-x)^{\frac{2}{3}} - \frac{1}{z-1}[1+(z-1)x]^{\frac{2}{3}} = \frac{2k_p t}{r_0^2} \quad (1)$$

where k_p is the rate constant, t is time, and $z = 1.53$ is the relative volume expansion when Ni reacts to form NiO. r_0 is the initial radius of nickel particle and x is the fraction of Ni that has oxidized (i.e., oxidation ratio).

Equation 1 was solved numerically using the average particle sizes measured by TEM. The fits look reasonable on a linear plot as shown in Fig. 5, especially in the case of Ni 79 nm and Ni 0.7 μm, for temperatures lower than 300°C. At higher temperatures particle sintering occurs, which produces agglomeration, and is expected to inhibit oxidation kinetics [11, 18]. Agglomeration was present at 350°C in Ni 79 nm. On the other hand, Ni 3 μm isotherms do not fit very well with the diffusion model at the initial stage of the reaction. The reaction appears to be too rapid during the early stages, due to the large surface area of irregularly shaped particles. During the last stages of the reaction the rate is too slow, first because the area available for oxidation decreases with time due to sintering/agglomeration [18], second because the formation of oxide layer hindered the further oxidation of particles [19], and third because grain growth during oxidation reduces the number of easy diffusion paths at the grain boundaries [8, 9, 20].

The oxidation rate constant k_p was determined from the fit in Fig. 5. The values range from 2.86×10^{-15} cm^2/s at 350°C to 2.86×10^{-17} cm^2/s at 250°C for Ni 79 nm, 5.83×10^{-16} cm^2/s to 9.49×10^{-18} cm^2/s for Ni 0.7 micron, and 7.17×10^{-17} cm^2/s to 2.10×10^{-18} cm^2/s for Ni 3 micron. The oxidation rate constant k_p is plotted against the inverse temperature for nickel 79 nm, 0.7 μm, and 3 μm in Fig. 6 and seen to fall within the limits reported for oxidation of bulk nickel [6]. Other values reported for oxidation of various nickel particle sizes are also shown for comparison [13–15]. Some results for bulk oxidation are present [8, 9, 20] as well as the values deduced from Ni diffusion in NiO [21].

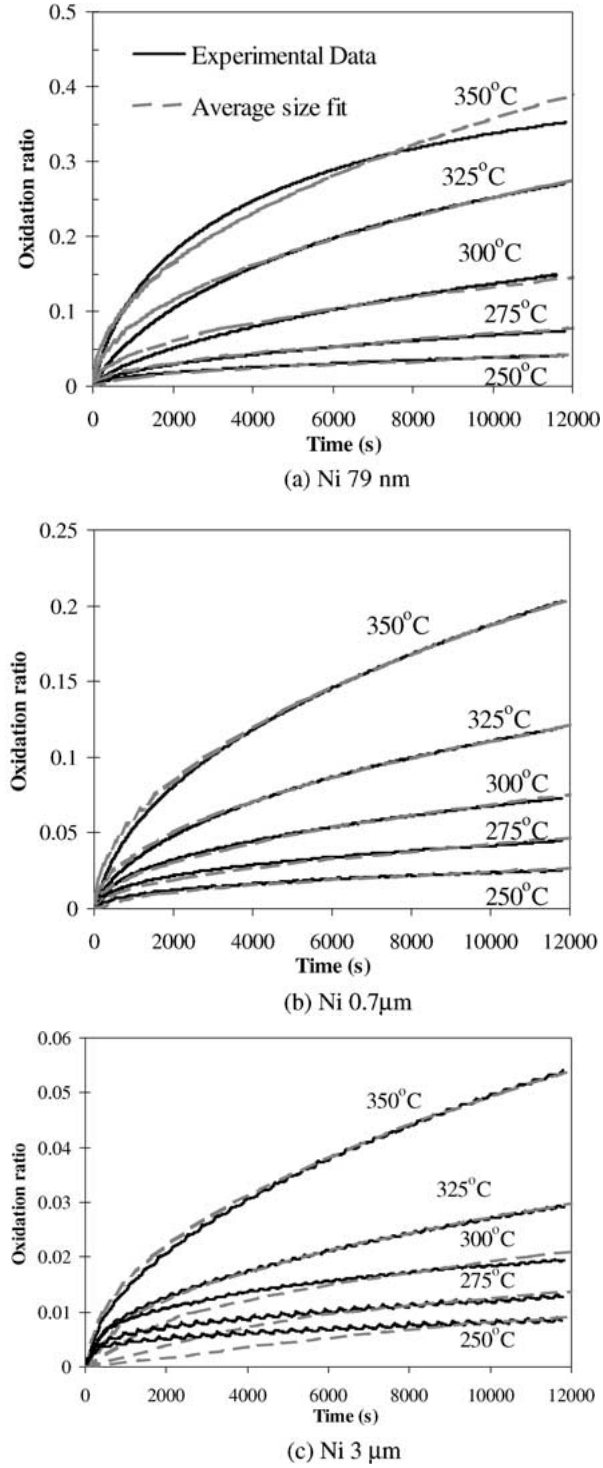

Figure 5 Least square fits of the experimental data at five temperatures, to a diffusion limited oxidation theory for spherical particles of 79 nm (a), 0.7 μm (b), and 3 μm (c).

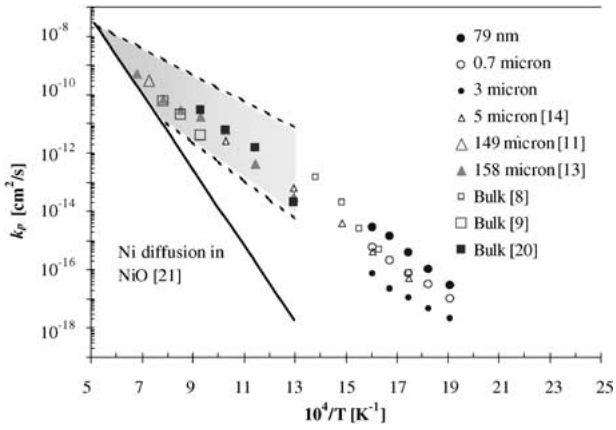

Figure 6 Oxidation rate constant k_p of nickel at different temperatures. The values for particles of different sizes (circles) fall within reported limits [6] for bulk oxidation (shaded area). Some results for nickel particles (triangulars) [11, 13, 14] and some results for bulk oxidation (squares) [8, 9, 20] are also shown for comparison.

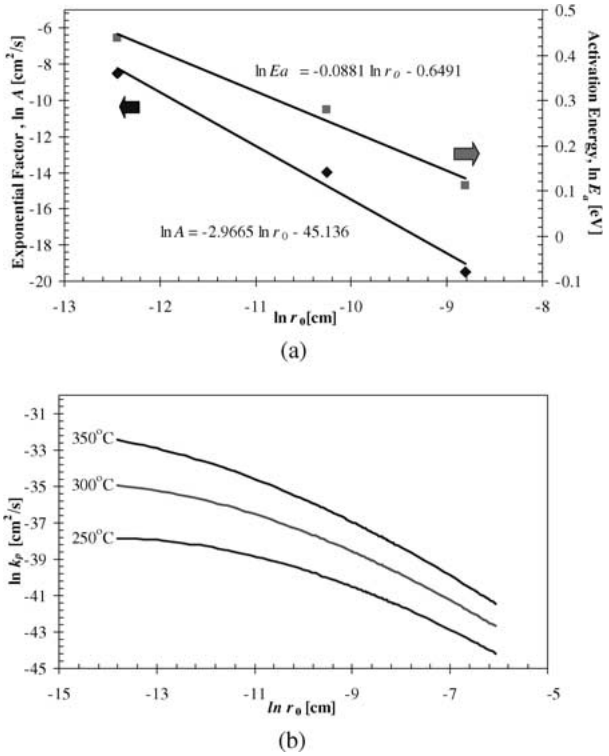

Figure 7 (a) The exponential factor (A) and the activation energy (E_a) are plotted against initial radius (r_0). Linear relationships to ln r_0 are found for both ln A and ln E_a curves. (b) Kinetic rate constant (k_p) is plotted against initial radius (r_0).

The rate constants vary greatly with temperature and are governed by the Arrhenius equation:

$$k_p = A\,\mathrm{e}^{-E_a/RT} \tag{2}$$

where R is the gas constant. Therefore, the temperature dependence of the rate constant is exponential, and governed by the value of the *experimental activation energy*, E_a. The constant A is usually called the *exponential factor* and can be obtained from an intercept of $\ln k_p$ versus $1/T$ plot. Both E_a and A vary greatly with particle size as illustrated in Fig. 7a. The particle size dependence may be expressed in logarithmic forms:

$$\ln E_a = -0.0881 \ln r_0 - 0.6491 \tag{3}$$

$$\ln A = -2.9665 \ln r_0 - 45.136 \tag{4}$$

where r_0 is initial radius of particle in cm. In case of the larger particle size, there are larger amounts of free surface that facilitates diffusion and lowers the value of the activation energy as illustrated in Equation 3. Substitution of Equations 3 and 4 into Equation 2 and rearrangement yields:

$$k_p = 2.50 \times 10^{-20} r_0^{-2.9665} \exp\left(\frac{0.523 r_0^{-0.0881}}{RT}\right) \tag{5}$$

Equation 5 summarizes the relationship between the oxidation rate constant and the initial radius (r_0). The kinetic constant is plotted against r_0 at three different temperatures in Fig. 7b. It indicates that nickel of smaller particle size has higher reactivity than nickel of larger particle size.

The thickness of the oxide layer after oxidation process can then be estimated. The instantaneous radius of unreacted Ni (r_1) [5] and the instantaneous radius of the sphere of product (r_2) [5] are calculated using Equations 6 and 7, respectively.

$$r_1 = (1-x)^{\frac{1}{3}} r_0 \tag{6}$$

$$r_2^3 = z r_0^3 + r_1^3 (1-z) \tag{7}$$

The thickness of the oxide layer (t_o) is equal to $r_2 - r_1$. The oxide layer measured from HRTEM of the oxidized particles is shown in Fig. 8. The diffusion-controlled model predicts thinner oxide layer than experiments. This can possibly be due to further oxidation of the particle or the agglomeration of oxidized particle after they were removed from the crucible. In order to compare the trend of the oxide growth of each particle size, the oxide layers are normalized by the initial particle radius and then plotted against oxidation temperature and oxidation ratio in Fig. 9. It is noticed that the smaller the particles, the higher the percentage of oxidation per volume that results in a thicker normalized oxide layer for the same oxidation temperature.

3.2. Oxidation maps

The oxidation ratio can be presented in terms of temperature and time as shown in the oxidation maps of Fig. 10. The oxidation map of each nickel particle size is obtained from solving Equation 1 numerically using rate constant found in the previous section. These plots are useful in determining the oxidation ratio of the nickel particles at various processing condition.

3.3. Effect of oxidation on magnetic properties

The magnetic properties of bare nickel particles are summarized in Table I. All nickel particles show the saturation magnetization (M_s) of 53.23 ± 0.571 emu/g which is closed to that of bulk nickel (55 emu/g). The bare nanoparticle (79 nm) samples have the largest coercivity of 111.52 ± 5.169 Oe while the other samples

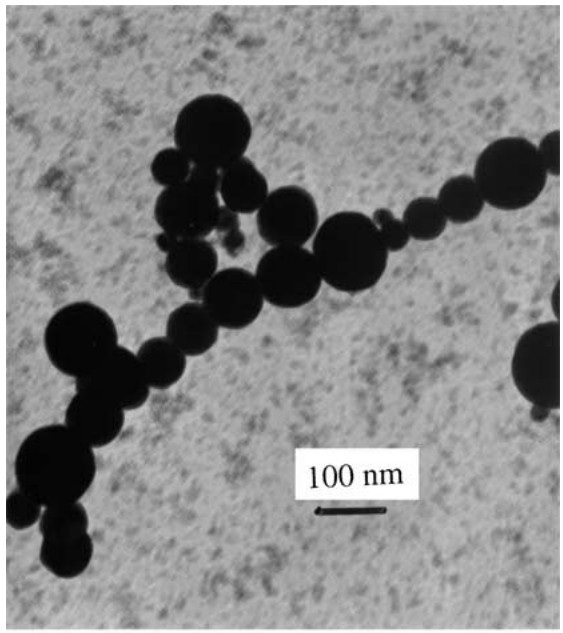

(a) Before oxidation

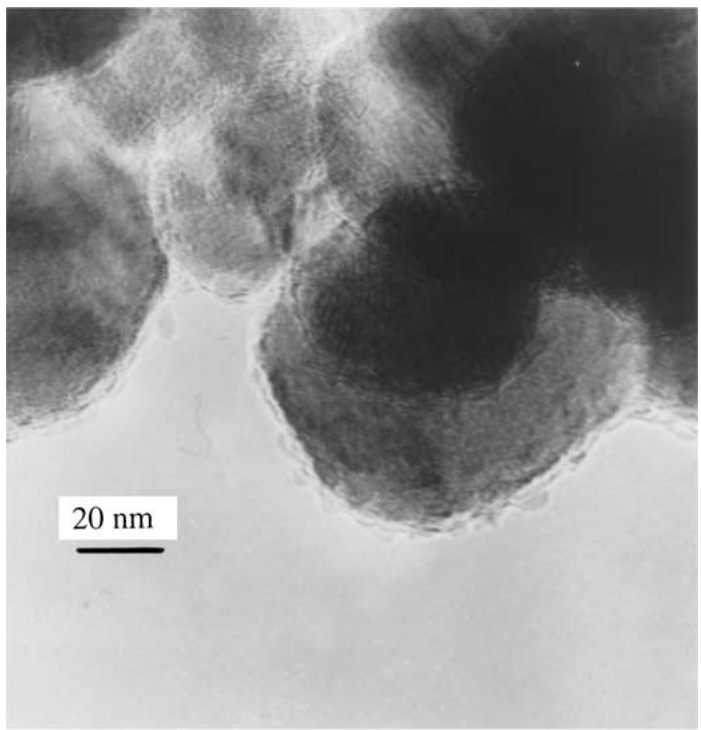

(b) After oxidation

Figure 8 The electron micrographs of Ni 79 nm shows the nickel particle before and after oxidation at 275°C in air for 3 hours. The oxide layer thickness is approximately 6 nm.

TABLE I Summary of magnetic properties of bare nickel particles

Particle size	Coercivity (H_c, Oe)	Saturation magnetization (M_s, emu/g)	Hysteresis loop area ($\times 10^3$ erg/g)
79 nm	111.52 (5.169)	53.01 (2.570)	12.37 (0.933)
0.7 micron	107.50 (1.513)	52.63 (1.563)	12.45 (1.561)
3 micron	82.36 (2.113)	53.63 (1.115)	8.26 (0.748)

coercivities range from 82.36 ± 2.113 to 107.50 ± 1.513 at room temperature. These results confirm that the coercivity (H_c) is strongly size dependent in fine particles [22–24].

Nickel ultrafine particles actively react with oxygen to form nickel oxide layers on the particle surfaces. On the other hand, a preoxidation step can improve the environmental stability of the ultrafine particles and promote adhesion between particles and polymer matrix. However, the formation of the oxide layers decreases the saturation magnetization and particle heating efficiency. Magnetization is a volume dependent magnetic property. The magnetization decreases as the oxidation temperature increases and resulting oxidation ratio increases as shown in Fig. 11. It is seen that it is more severe in the smaller particle size due to the larger percentage of oxide volume.

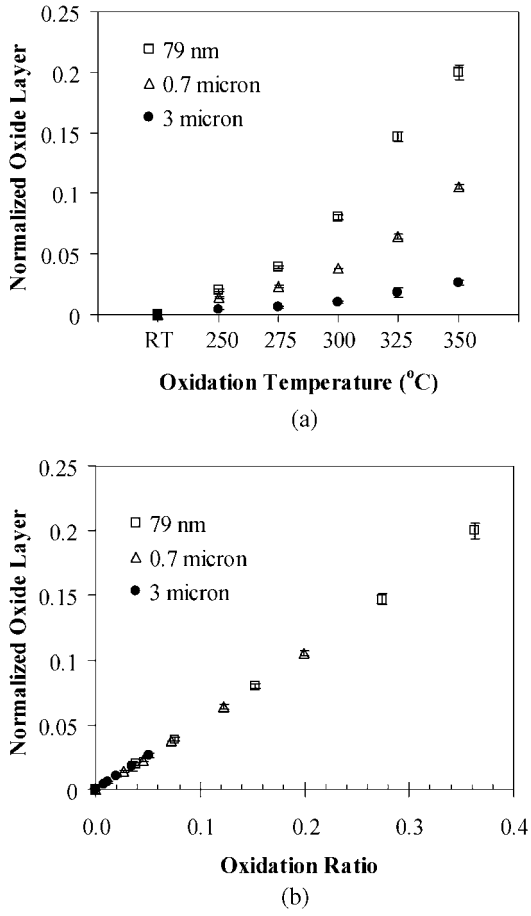

Figure 9 Normalized oxide layer of Ni particles after oxidation in air for 3 hours plotted against oxidation temperatures (a) and oxidation ratio (b).

Fig. 11b clearly shows that the normalized magnetization (M/M_0) is linearly proportional to the normalized volume of unreacted Ni. The equation for magnetization as a function of oxidation ratio can be written from Fig. 11 and Equation 6 as follow:

$$\frac{M}{M_0} = 1.53\left(\frac{r_1^3}{r_0^3}\right) - 0.53 \tag{8}$$

where M is magnetization of Ni particle at any time, M_0 is the saturation magnetization of Ni at room temperature. Substitution of $z = 1.53$, the relative volume expansion when Ni reacts to form NiO, into Equation 8 and rearrange using Equation 6 yields

$$\frac{M}{M_0} = 1 - zx \tag{9}$$

M/M_0 can also be expressed in term of r_2 by substituting Equation 7 into Equation 8.

$$\frac{M}{M_0} = \frac{z}{1-z}\left(\frac{r_2^3}{r_0^3}\right) - \left(\frac{z}{1-z} + (1-z)\right) \tag{10}$$

Equation 10 is plotted and compared with the experimental data in Fig. 12.

Interestingly, Fig. 13 presents a different influence of oxidation on coercivity. It is shown here that oxide layers improve the coercivity of nickel particle and then

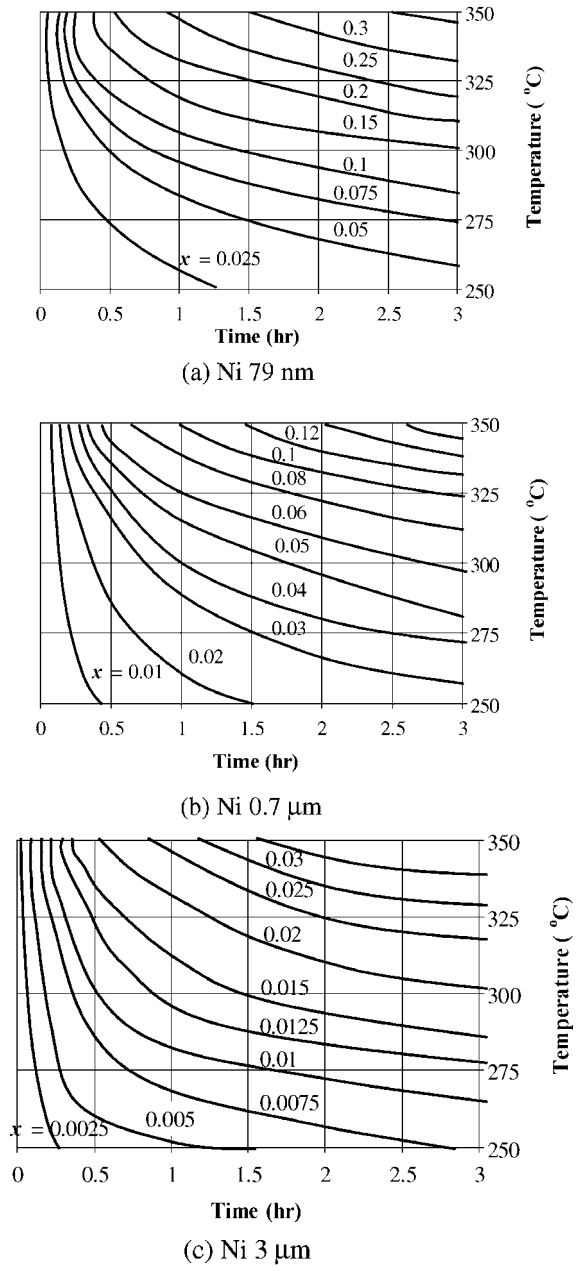

Figure 10 Oxidation maps show the oxidation ratios (x) as a function of temperature and exposure time for nickel 79 nm (a), 0.7 μm (b), and 3 μm (c).

drop off. The coercivity depends not only on the particle size, shape and surface treatments but also on the packing and orientation states of particles [25, 26]. If it is assumed that there are constant numbers of grains in the particle of the same size, the oxidation obviously affect the size of grains being subjected to an applied magnetic field. At the initial state the magnetic moments are randomly distributed in the domains. As the oxidation proceeds, the volume of the unreacted Ni decreases while the numbers of the grains remain the same. This results in restricted space for magnetic moments and higher energy required in hysteresis interaction with an applied field. The materials lose their magnetic properties when the oxidation has reached the state where the reduce grain sizes inhibit the movement of the magnetic moments.

Oxidation has a severe effect on the magnetic properties of ultrafine nickel particles and consequently affects

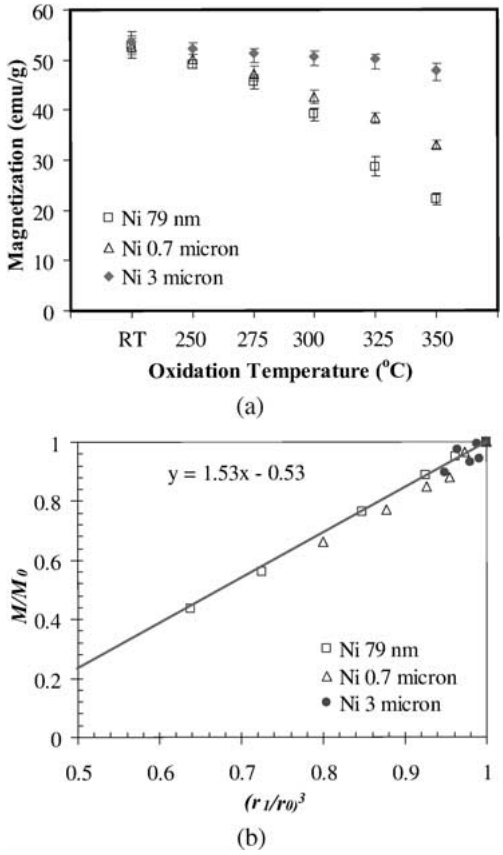

Figure 11 Magnetization of oxidized Ni particle plotted against oxidation temperatures (a) and volume of unreacted Ni (b). r_1 is the radius of unreacted Ni and r_0 is the initial radius.

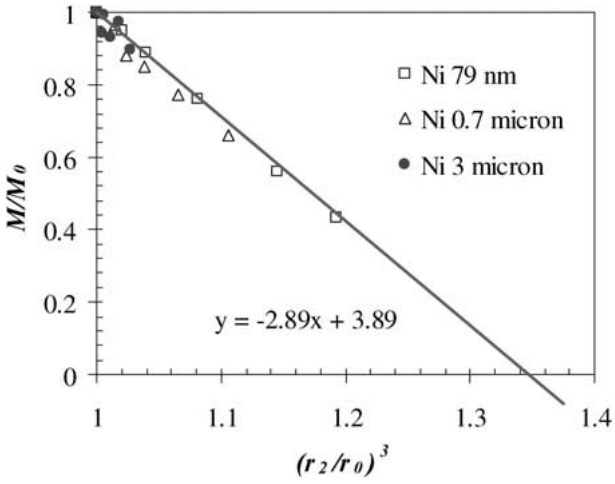

Figure 12 Magnetization of oxidized Ni particle plotted against normalized particle size. Equation 10 (solid line) seems to have good agreement with the experimental data. r_2 is the instantaneous radius of the sphere of product and r_0 is the initial radius.

the particle heating efficiency. As discussed elsewhere [1], the characteristic-heating rate of nickel can be estimated from DC saturation hysteresis loop,

$$E_{hs} = \beta \mu_0 M_s H_s, \tag{11}$$

where H_s is the field strength required to saturate the hysteresis loop. β is a constant and μ_0 is permeability in free space. If it is assumed that the shape of the hysteresis loop is the same for oxidized particles and

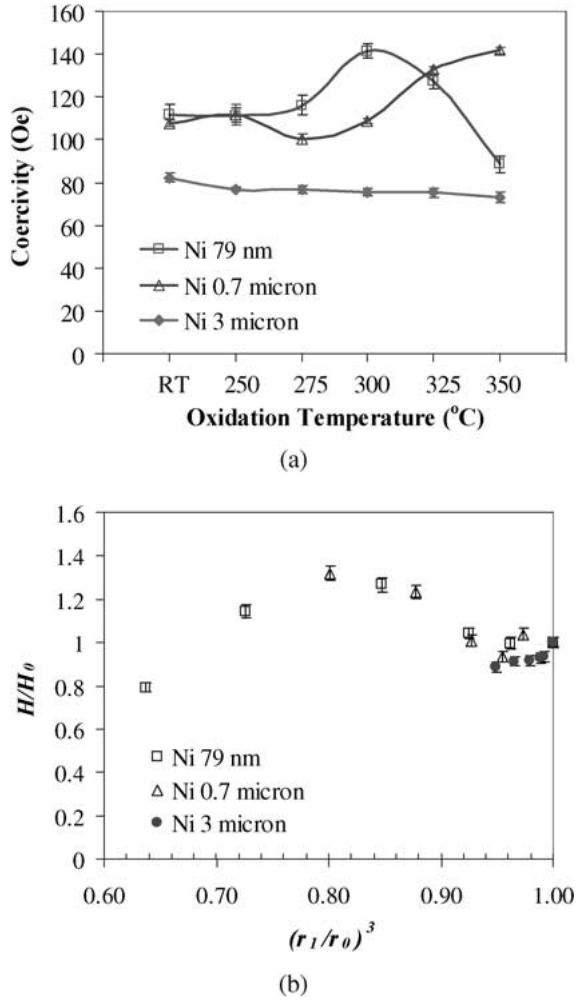

Figure 13 Coercivity of oxidized Ni particle plotted against oxidation temperatures (a) and volume of unreacted Ni (b).

unoxidized ones, E_{h0}, hysteresis loop area after oxidation, can be written as:

$$E_{hs} = \beta \mu_0 M H_p \tag{12}$$

where H_p is the applied field strength and is the same as H_s. Then the ratio of hysteresis loop area of oxidized particles over bare particles is then shown as:

$$\frac{E_{h0}}{E_{hs}} = \frac{M}{M_0} \cdot \frac{H_p}{H_s} \tag{13}$$

$$\frac{E_{h0}}{E_{hs}} = 1 - zx \tag{14}$$

The relationship between the relative hysteresis energy loss and the oxidation ratio is shown in Equation 14. The combination of oxidation maps in Fig. 10 and the relative hysteresis energy loss in Equation 11 results in heating efficiency maps for nickel particles as a function of oxidation conditions, as shown in Fig. 14. In combination, the oxidation maps of Fig. 10 and heating efficiency maps of Fig. 14 are useful tools in predicting the particle heating efficiency and optimizing the processing conditions for fabrication of Ni particulate loaded polymers.

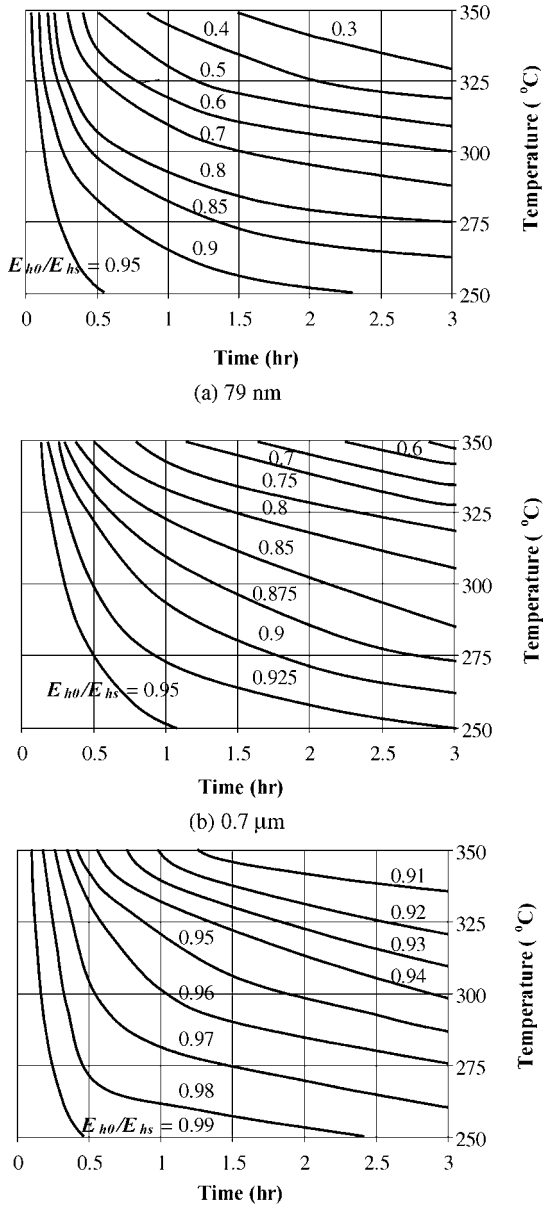

Figure 14 The relative hysteresis energy loss (E_{h0}/E_{hs}) is plotted as a function of oxidation temperature and time for nickel 79 nm (a), 0.7 μm (b), and 3 μm (c).

4. Conclusions

The oxidation of nickel particles of various sizes in the temperature range between 250°C and 350°C can be described by diffusion-controlled mechanisms proposed by Carter [11]. The oxidation kinetics deviate from the diffusion-controlled model during the initial stages of 3-μm nickel particles due to large surface area of irregularly shaped particles and during the last stages of 79-nm nickel particles at temperature above 300°C due to particle sintering. Estimated rate constants were compared with the previous results [13–15] and found to fall within the limits reported for oxidation of bulk nickel [6]. The activation energies of metal oxidation are approximately 1.55 eV, 1.32 eV and 1.12 eV for Ni 79 nm, Ni 0.7 μm and Ni 3 μm, respectively and the exponential factor demonstrates particle size dependence. The oxidation effect on the magnetic properties of the nickel particles is found to be significant. The saturation magnetization reduced volumetrically with unreacted nickel. The oxidation effect on coercivity is discussed in terms of grain size reduction. A guideline for nickel particulate loaded thermoplastic processing is established through the process-structure-performance relationships in the form of oxidation maps and heating efficiency maps.

Acknowledgements

The authors wish to thank Dr. John Q. Xiao and Yunfei Li at the Physics and Astronomy Department, University of Delaware for their assistance on magnetic property analysis and x-ray diffraction experiments. Partial financial support from the Ministry of Science, Technology and Environment, the Royal Thai Government is acknowledged. This research was also partially sponsored by the Army Research Laboratory (ARMAC-RTP) and was accomplished under the ARMAC-RTP Cooperative Agreement Number DAAD19-01-2-001. The views and conclusions contained in this document are those of the authors and should not be interpreted as representing official policies, either expressed or implied, of the Army Research Laboratory or the U.S. Government. The U.S. Government is authorized to reproduce and distribute reprints for Government purposes notwithstanding any copyright notation hereon.

References

1. E. WETZEL and B. K. FINK, ARL-TR-2431, U.S. Army Research Laboratory, Aberdeen Proving Ground, MD, March 2001.
2. V. LEGER, C. RAMIARINJAONA, R. BARRUE and R. LEBOURGEOIS, *J. Magn. Magn. Mater.* **191** (1999) 169.
3. T. H. McGAFFIGAN, U.S. Patent No. 5,208,443, 1993.
4. Y. A. MONOVOUKAS, U.S. Patent No. 5,378,879, 1995.
5. A. T. FROMHOLD Jr., "Theory of Metal Oxidation" (North-Holland, Amsterdam, 1976) Vol. 1.
6. A. ATKINSON, *Rev. Mod. Phys.* **57** (1985) 437.
7. R. GHEZ, *J. Chem. Phys.* **58** (1973) 1838.
8. M. J. GRAHAM and M. COHEN, *J. Electrochem. Soc.* **119** (1972) 879.
9. F. N. RHINES and R. G. CONNELL Jr., *ibid.* **124** (1977) 1122.
10. N. CABRERA and N. F. MOTT, *Rep. Prog. Phys.* **12** (1948/1949) 163.
11. R. E. CARTER, *J. Chem. Phys.* **34** (1961) 2010.
12. A. T. FROMHOLD, Jr., *J. Phys. Chem. Solids* **49** (1988) 1159.
13. R. KARMHAG, G. A. NIKLASSON and M. NYGREN, *J. Mater. Res.* **14** (1999) 3051.
14. *Idem.*, *J. Appl. Phys.* **85** (1999) 1186.
15. R. KARMHAG *et. al.*, *Solar Energy* **68**(4) (2000) 329.
16. W. J. TSENG, C.-K. HSU, C.-C. CHI and K.-H. TENG, *Mat. Let.* **52** (2002) 313.
17. A. ATKINSON and R. I. TAYLOR, *Philos. Mag.* A **43** (1981) 979.
18. T. WERBER, *Solid State Ionics* **42** (1990) 205.
19. A. DEGEN, J. MACEK and B. NOVOSEL, *J. Therm. Anal.* **48** (1997) 657.
20. A. ATKINSON, R. I. TAYLOR and A. E. HUGHES, *Philos. Mag.* A **45** (1982) 823.
21. A. ATKINSON and R. I. TAYLOR, *ibid.* **39** (1979) 581.
22. B. D. CULLITY, "Introduction to Magnetic Materials" (Addison-Wesley, Reading, MA, 1972).
23. Y.-W. DU *et. al.*, *J. Appl. Phys.* **70** (1991) 5903.
24. P. SARAVANAN, T. A. JOSE, P. J. THOMAS and G. U. KULKARNI, *Bulletin of Materials Science (India)* **24** (2001) 515.
25. G. BOTTONI, D. CANDOLFO, M. CECCHETTI, A. R. CORRADI and F. MASOLI, *J. Magn. Magn. Mater.* **120** (1993) 167.
26. X. Q. ZHAO, Y. LIANG, Z. Q. HU and B. X. LIU, *J. Appl. Phys.* **80** (1996) 5857.

Received 6 November 2001
and accepted 26 August 2002